A Memetic-Driven Multi-objective Sparse Unmixing Method for Hyperspectral Image

1st Zidong Wu
Xidian University
Xi'an, China
24021211429@stu.xidian.edu.cn

2nd Xiangming Jiang*
Xidian University
Xi'an, China
xmjiang@xidian.edu.cn

3rd Xiaolong Fan
Xidian University
Xi'an, China
xiaolongfan@outlook.com

4th Mingyang Zhang
Xidian University
Xi'an, China
myzhang@xidian.edu.cn

5th Jianzhao Li
Xidian University
Xi'an, China
ljz@ieee.org

6th Maoguo Gong
Xidian University
Xi'an, China
gong@ieee.org

***Abstract*—This paper presents a novel memetic hyperspectral unmixing approach based on the MOEA/D framework, focusing on endmember identification using a spectral library. The population is optimized by alternately applying genetic and local search operators. The local search operator is designed to extract and utilize knowledge accumulated across iterations, particularly the endmember abundances of each individual. This enables it to guide individual optimization toward the direction dictated by cultural genes. Additionally, a voting mechanism integrates multiple Pareto-optimal solutions by selecting the most frequently occurring endmembers as the final set, thereby mitigating the instability inherent in relying on a single solution. Extensive experiments on simulated and real datasets demonstrate that incorporating cultural genes significantly enhances the evolutionary algorithm's performance, yielding superior unmixing results.**

***Index Terms*—Hyperspectral unmixing, MOEA/D, memetic approach, local search operator, voting mechanism.**

I. INTRODUCTION

With the rapid advancement of aerospace and spectral imaging techniques, the field of hyperspectral image unmixing has witnessed significant breakthroughs [1]. Hyperspectral images contain not only spatial distribution information of ground objects but also rich spectral features, such as absorption and scattering characteristics of different materials. This endows hyperspectral images with unique advantages in ground target recognition, surpassing other types of images [2]. Moreover, the rich spectral information has unlocked new possibilities in numerous application areas, such as environmental monitoring, urban risk prevention, and mineral exploration. However, due to the limited spatial resolution and the micro-level mixture of ground substances, hyperspectral images are often composed of mixed spectra. The core objective of hyperspectral unmixing is to extract the pure spectra (endmembers) of the constituent materials from the mixed spectra and estimate the proportion (abundance) of each material [3].

There are numerous hyperspectral image unmixing methods, with traditional approaches, deep learning methods, and evolutionary computation methods being particularly prominent. Traditional hyperspectral unmixing typically revolve around linear [4] and nonlinear mixture paradigms [5], requiring the selection of appropriate methods and models based on specific application scenarios [6]. The optimization process can utilize features such as spectral subspace similarity [7] or the piecewise smoothness of abundance maps [8]. While traditional unmixing methods have achieved significant results in the field, they remain limited in their ability to capture global spatial information, adapt flexibly to diverse scenarios, and handle complex optimization problems.

Benefiting from the powerful learning capabilities of deep neural networks [9], deep learning methods for hyperspectral unmixing have advanced in recent years. One of the most widely used networks in this field is the autoencoder (AE) [10], which maps hyperspectral data to a low-dimensional space (corresponding to the representation of endmembers and abundances) to reconstruct the spectra [11]. Researchers have enhanced AE in various ways: diffusion models were first introduced to unmixing by [12]. Gao et al. preserved spatial information through cascading and convolution operations, enabling richer feature learning [13]. and Su et al. proposed a deep autoencoder-augmented network (DAAN) that employs a multilinear mixture model to address nonlinear effects from multiple scattering [14]. Compared to traditional methods, deep learning methods show clear advantages in handling complex nonlinear relationships and scalability.

Evolutionary computation methods for unmixing often integrate genetic algorithms, particle swarm optimization, and multi-objective optimization techniques. Li et al. segmented hyperspectral images into multiple homogeneous regions and modeled the unmixing task in each region as a multi-objective optimization problem, enabling information exchange between tasks to enhance the convergence speed [15]. The same group addressed the problem from another angle by modeling abundance, spatial, and temporal constraints as three separate objectives, which were dynamically combined via a sub-fitness-based multi-objective evolutionary approach to produce optimal sub-pixel classification maps [16]. These studies illustrate that evolutionary computation is well-suited

This work was supported by the Natural Science Basic Research Program of Shaanxi under Grant No. 2025CY-YBXM-049.

for integration with multi-objective optimization. Compared to traditional unmixing methods, evolutionary multi-objective algorithms are better adapted to complex, dynamic scenarios; compared to deep-learning methods, they provide greater interpretability in both optimization process and results. However, most existing evolutionary unmixing algorithms do not fully exploit the information obtained during the population evolution process. Although Li et al. mentioned that information sharing between tasks can improve unmixing efficiency [15], they overlooked the information carried by individuals during intra-task evolution. Likewise, many methods only preserve the final optimal solution set, discarding the information accumulated throughout the search process. To better utilize individual information, this paper proposes a memetic algorithm that collects and integrates such information to construct local search operators, thereby further improving population evolution.

The memetic algorithm integrates global search with local optimization [17], demonstrating excellent performance in handling various complex optimization problems [18], [20], [21]. Its core concept combines features of genetic algorithms and cultural learning, operating on the principle of transmitting and accumulating valuable information within the population through the interaction of genetic and cultural genes. General steps include gene expression strategies, individual initialization, selection and mutation, population update, repeated evolution, and iteration termination. Collecting abundance information carried by individuals during optimization helps refine the direction of endmember selection.

In terms of solution strategy, this paper utilizes the method proposed in [19] which determines the number of endmembers by identifying the knee point on the Pareto front. A voting mechanism is then designed to identify the most significant endmembers, evaluated based on the frequency with which they are selected by Pareto optimal solutions. Finally, based on the predetermined number of endmembers, the set of endmembers with the highest frequency is chosen as the final solution. This voting mechanism integrates the identification capabilities of multiple Pareto optimal solutions, thereby avoiding the instability associated with relying on a single solution. Consequently, it enhances the robustness and representativeness of the identified endmembers.

The structure of this paper is as follows: Section 2 introduces the hyperspectral mixture model and the design of multi-objective hyperspectral unmixing model. Section 3 presents the framework of MOEA/D, the design of the local search operator, the solution selection strategy, and the voting mechanism. Section 4 analyzes the performance on both synthetic and real datasets. Section 5 provides concluding remarks.

II. Hyperspectral Unmixing and Evolutionary Multi-objective Models

A. Sparse hyperspectral unmixing

In the case of the linear mixing mechanism, the hyperspectral image can be approximately expressed as a linear combination of a series of endmembers, i.e.,

$$\begin{aligned} &\boldsymbol{Y}=\boldsymbol{M}\boldsymbol{S}+\boldsymbol{N} \\ \text{subject to}\quad &\boldsymbol{S}\geq \boldsymbol{0}, \boldsymbol{1}_{\boldsymbol{q}}^{\boldsymbol{T}}\boldsymbol{S}=\boldsymbol{1}_{\boldsymbol{n}}^{\boldsymbol{T}} \end{aligned} \tag{1}$$

where $\boldsymbol{Y}$ has dimensions $L \times n$, representing the rearranged hyperspectral image with L spectral bands and n pixels. $\boldsymbol{M}$ is an $L \times p$ dimensional matrix, with p denoting the number of endmembers. $\boldsymbol{S}$ is a $p \times n$ matrix, indicating the abundance of each endmember in each pixel. $\boldsymbol{N}$ represents the modeling error and noise. To make the linear mixing model more realistic, the non-negative and sum-to-one constraints are imposed on the abundance matrix $\boldsymbol{S}$ in model (1). These constraints require that the abundances of all endmembers in a pixel must be non-negative and their sum must equal to 1.

Linear hyperspectral unmixing is the inverse process of model (1) and consists of two tasks: endmember extraction and abundance estimation. This process is a bilinear optimization problem. With the establishment and improvement of spectral libraries, researchers have proposed methods to simplify the unmixing process. One such method assumes that all endmembers in the hyperspectral image $\boldsymbol{Y}$ are contained within an over-complete spectral library $\boldsymbol{A}$ with dimensions $L \times q\,(q \gg p)$. Therefore, the estimation of the endmember matrix $\boldsymbol{M}$ and the abundance matrix $\boldsymbol{S}$ can be regarded as a sparse regression problem of the hyperspectral image $\boldsymbol{Y}$ with respect to the library $\boldsymbol{A}$. Assuming the regression coefficient matrix is $\boldsymbol{X}$, this relationship can be expressed as

$$\begin{aligned} &\boldsymbol{Y}=\boldsymbol{A}\boldsymbol{X}+\boldsymbol{N} \\ \text{subject to}\quad &\boldsymbol{X}\geq \boldsymbol{0}, \boldsymbol{1}_{\boldsymbol{q}}^{\boldsymbol{T}}\boldsymbol{X}=\boldsymbol{1}_{\boldsymbol{n}}^{\boldsymbol{T}} \end{aligned} \tag{2}$$

Due to the over-completeness of spectral library $\boldsymbol{A}$ and the correlation between spectral features, solving for matrix $\boldsymbol{X}$ in (2) is generally an ill-posed problem. Regularization constraints on $\boldsymbol{X}$ are needed to obtain a meaningful solution. Assuming the endmember matrix $\boldsymbol{M}$ is included in $\boldsymbol{A}$ and the number of endmembers p is much smaller than the number q, the coefficient matrix $\boldsymbol{X}$ for hyperspectral image $\boldsymbol{Y}$ with respect to $\boldsymbol{A}$ should be sparse. Thus, the sparse unmixing model for (2) can be established as

$$\begin{aligned} \min_{\boldsymbol{X}}\quad &\frac{\boldsymbol{1}}{\boldsymbol{2}}\|\boldsymbol{Y}-\boldsymbol{A}\boldsymbol{X}\|_F^2+\lambda\|\boldsymbol{X}\|_{2,0} \\ \text{subject to}\quad &\boldsymbol{X}\geq \boldsymbol{0},\ \boldsymbol{1}_{\boldsymbol{q}}^{\boldsymbol{T}}\boldsymbol{X}=\boldsymbol{1}_{\boldsymbol{n}}^{\boldsymbol{T}} \end{aligned} \tag{3}$$

where $\|\boldsymbol{X}\|_{\boldsymbol{2,0}}=\left\|\sqrt{\sum_{\boldsymbol{j=1}}^{\boldsymbol{n}}\boldsymbol{X}_{\boldsymbol{i,j}}^{\boldsymbol{2}}}\right\|_{\boldsymbol{0}}$ is the regularization term that induces row sparsity in matrix $\boldsymbol{X}$, and λ is the regularization parameter. To simplify the problem-solving process, researchers often relax the l_0-norm to the l_1-norm. Moreover, $\|\boldsymbol{X}\|_{\boldsymbol{2,1}}=\left\|\sqrt{\sum_{\boldsymbol{j=1}}^{\boldsymbol{n}}\boldsymbol{X}_{\boldsymbol{i,j}}^{\boldsymbol{2}}}\right\|_{\boldsymbol{1}}$ also induces row sparsity in the matrix, and the model is transformed to

$$\begin{aligned} \min_{\boldsymbol{X}}\quad &\frac{1}{2}\|\boldsymbol{Y}-\boldsymbol{A}\boldsymbol{X}\|_F^2+\lambda\|\boldsymbol{X}\|_{2,1} \\ \text{subject to}\quad &\boldsymbol{X}\geq \boldsymbol{0},\ \boldsymbol{1}_{\boldsymbol{q}}^{\boldsymbol{T}}\boldsymbol{X}=\boldsymbol{1}_{\boldsymbol{n}}^{\boldsymbol{T}} \end{aligned} \tag{4}$$

B. Multitobjective Endmember Extraction Model

The multitobjective endmember extraction model is established based on model (3). Given a known hyperspectral image $\boldsymbol{Y}$ and an over-complete spectral library $\boldsymbol{A}$, assume $\boldsymbol{A}$ contains q endmembers. We can use an q-dimensional vector $\boldsymbol{I} = \{I_1, I_2, \ldots, I_q\}$, where $I_i \in \{0, 1\}$, to indicate whether the endmember in $\boldsymbol{A}$ is present in $\boldsymbol{Y}$. The multiobjective endmember extraction model can be reestablished [19] as

$$\min_{\boldsymbol{I}\in\{0,1\}^n} \boldsymbol{F(I)} = \{\|\boldsymbol{Y} - \boldsymbol{A_I X_I}\|_F^2, \|\boldsymbol{I}\|_0\} \tag{5}$$

where the first objective in model (5) represents the unmixing residual termed RSE1, while the second objective represents the number of identified endmembers termed SP1. $\boldsymbol{I}$ is composed of 0 and 1. The columns of $\boldsymbol{A}$ corresponding to the non-zero elements in $\boldsymbol{I}$ are extracted to form the matrix $\boldsymbol{A_I}$. $\boldsymbol{X_I}$ represents the projection of $\boldsymbol{Y}$ onto $\boldsymbol{A_I}$, given by:

$$\boldsymbol{X_I} = \left(\boldsymbol{A_I^T A_I}\right)^{-1} \boldsymbol{A_I^T Y} \tag{6}$$

The model (5) can be solved using the MOEA/D framework which will be briefly reviewed below. To effectively recombine binary-encoded individuals during the evolution process, this paper utilizes a multi-point crossover operator. Meanwhile, to introduce new genes and maintain population diversity, a single-point mutation operator is applied.

C. Abundance Estimation Section

By solving the model (5), the optimal solution $\boldsymbol{I_{opt}}$ can be obtained. Using $\boldsymbol{I_{opt}}$, the true endmembers in $\boldsymbol{A}$ can be located, denoted as $\boldsymbol{M} = \boldsymbol{A_{I_{opt}}}$. Once the endmember matrix $\boldsymbol{M}$ is determined, the abundance estimation problem can be transformed into solving the equation $\boldsymbol{Y} = \boldsymbol{MX}$, where $\boldsymbol{X}$ is the abundance matrix to be solved, satisfying $\boldsymbol{X} \geq \boldsymbol{0}$. This problem can be solved using the SUnSAL-TV algorithm [23], which is mathematically expressed as follows:

$$\min_{\boldsymbol{X}\geq\boldsymbol{0}} \quad \frac{\boldsymbol{1}}{\boldsymbol{2}}\|\boldsymbol{Y} - \boldsymbol{MX}\|_F^2 + \boldsymbol{\lambda}_{\text{TV}} \boldsymbol{TV(X)} \tag{7}$$

Here, $\|\cdot\|_F$ denotes the Frobenius norm of a matrix, λ_{TV} is a regularization parameters, and $\boldsymbol{TV(X)}$ represents the total variation regularization term, which introduces spatial correlation during abundance estimation and suppresses noise to enhance the quality and stability of the results.

III. Memetic algorithm under the MOEA/D Framework

A. Principle and Framework of MOEA/D

This paper employs the MOEA/D to solve the unmixing model (5). The core idea of MOEA/D is to transform a multi-objective optimization problem into a series of single-objective subproblems. Through the interaction among neighboring subproblems, these subproblems are collaboratively optimized to approach the entire Pareto solutions.

The aggregation function used is the Tchebycheff approach, which transforms a multiobjective optimization problem into a set of single-objective optimization problems as follow

$$\begin{aligned} &\min \ \boldsymbol{g^{te}(I \mid \lambda, z^*)} = \max_{1\leq i\leq m} \left\{\lambda^i |f_i(\boldsymbol{I}) - z_i^*|\right\}, \\ &\text{subject to} \quad \boldsymbol{I \in \Omega} \end{aligned} \tag{8}$$

where $\boldsymbol{z^*} = (z_1^*, \ldots, z_m^*)$ is the reference point, and for $\forall i = 1, \ldots, m$, it is set as $z_i^* = \min\{f_i(\boldsymbol{I}) \mid \boldsymbol{I} \in \Omega\}$

Algorithm 1 MOEA/D Algorithm Framework

Input: Population size $\boldsymbol{P}$, neighborhood size $\boldsymbol{TN}$
Output: Approximate Pareto optimal solution set $\boldsymbol{PS}$, approximate Pareto front $\boldsymbol{PF}$

1: Generate weight vectors $\{\boldsymbol{\lambda_i}\}_{\boldsymbol{i=1}}^{\boldsymbol{P}}$ evenly distributed between $(0, 1)$ and $(1, 0)$.
2: Generate a series of scalarized subproblems with (8).
3: Search for neighboring subproblems for the i-th subproblem based on Euclidean distance, obtaining index $B(i)$.
4: Initialize the population $\{\boldsymbol{I_i}\}_{\boldsymbol{i=1}}^{\boldsymbol{P}}$, $\boldsymbol{PS} = \boldsymbol{PF} = \boldsymbol{\emptyset}$, and $\boldsymbol{z^*} = \min\{\boldsymbol{f}(\boldsymbol{I}_i) \mid \boldsymbol{i = 1, 2, \ldots, P}\}$.
5: **while** termination conditions are not met **do**
6:   **for** $\boldsymbol{i = 1 \to P}$ **do**
7:     Generate a new individual $\boldsymbol{\hat{I}_i}$ using genetic operators.
8:     Improve $\boldsymbol{\hat{I}_i}$ using a local search operator.
9:     Update the reference point $\boldsymbol{z^*}$.
10:     if $\boldsymbol{g(\hat{I}_i \mid \lambda_i, z^*)} \leq \boldsymbol{g(I_j \mid \lambda_j, z^*)}$, $\boldsymbol{j} \in \boldsymbol{B(i)} \cup \boldsymbol{i}$, then $\boldsymbol{I_j} = \boldsymbol{\hat{I}_i}$, $\boldsymbol{f(I_j)} = \boldsymbol{f(\hat{I}_i)}$.
11:     Update $\boldsymbol{PS}, \boldsymbol{PF}$.
12:   **end for**
13: **end while**

Most researchers introduce various methods at step 7 and 8 to attempt to obtain better solutions. Once the optimal solution is achieved, they will discard the previous solutions. In fact, they overlook that the solutions in each generation can carry valuable information. In fact, the abundance information corresponding to each individual $\boldsymbol{\hat{I}_i}$ in step 7 can be utilized to guide the subsequent direction of endmember selection.

B. Design of Local Search Operators

The above content describes the general steps of the MOEA/D framework in the endmember extraction process. During the optimization process of model (5), abundance is roughly estimated for each individual using the least squares method, but this abundance information is discarded after the evaluation of individuals, and thus is not fully utilized. Sparse regularized unmixing models indirectly achieve the goal of endmember selection by inducing the sparsity of $\boldsymbol{X}$, and the sparsity regularization of $\boldsymbol{X}$ is solved using a threshold truncation method. This inspired us to leverage threshold truncation to guide the endmember extraction process, thereby constructing the local search operator.

This concept functions similar to the model (4). In model (4), the term $\|\boldsymbol{X}\|_{2,1}$ serves the same role as $\|\boldsymbol{I}\|_0$. The 0-1 vector $\boldsymbol{I}$ is only used for endmember selection, while the abundance matrix $\boldsymbol{X}$ is used for both endmember selection and abundance estimation. Thus, the structure of $\boldsymbol{X}$ ensures that the number of its zero rows corresponds to the number of unselected endmembers. Based on this, $\boldsymbol{X}$ can be updated during the optimization of model (5), and further utilized to guide the construction of the local search operator.

In terms of specific operations, the abundance matrix $\boldsymbol{X_I}$ corresponding to each individual $\boldsymbol{I}$ is calculated. In order to utilize the abundance matrix $\boldsymbol{X_I}$ to perform local optimization on $\boldsymbol{I}$, the threshold truncation model can be establised as

$$\min_{\boldsymbol{X}} \quad \|\boldsymbol{X}\|_{2,1} + \lambda_2 \|\boldsymbol{X} - \boldsymbol{X_I}\|_F^2 \tag{9}$$

It should be noted that model (9) is introduced as a motivating surrogate rather than a subproblem that is exactly solved in each local-search step. The term $\|X\|_{2,1}$ promotes row sparsity and thus encourages the removal of weakly contributing endmembers, while the quadratic term $\|X - X_I\|_F^2$ constrains the updated abundance structure to remain close to the current estimate X_I. Therefore, rows with small ℓ_2 norms in X_I are more likely to correspond to insignificant endmembers and are natural candidates for pruning. From this perspective, the proposed rule can be viewed as a practical strategy inspired by the row-sparsity effect of model (9), rather than an exact proximal update or a standard one-step ISTA scheme.

Then, the l_2-norm of each row of $\boldsymbol{X_I}$ is computed. The row with the smallest l_2-norm is probabilistically set it to zero. Its corresponding index in $\boldsymbol{I}$ is

$$\boldsymbol{j} = \arg\min_{i} \|\mathbf{X_{I}}_i\|_2 \tag{10}$$

Therefore, the j-th element of $\boldsymbol{I}$ is set to zero with a certain probability. The illustration of the local search operator can be found in Fig. 1. Through trials, we have adaptively adjusted the zero-setting probability proportional to the weight used for constructing the subproblem. This is because the smaller the $\|\boldsymbol{I}\|_0$ of the corresponding subproblem is, the smaller the weight λ_2 should be, which indicates that the subproblem needs more sparsity for better solutions.

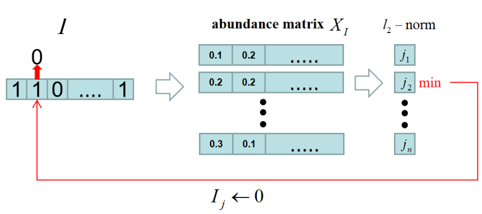

Fig. 1. Illustration on the local search operators

C. Voting solution strategy

When $\|\boldsymbol{I}\|_0$ is relatively large, the number of selected endmembers in $\boldsymbol{I}$ far exceeds the true number of endmembers in $\boldsymbol{Y}$, the unmixing error RSE1 will be very small. As $\|\boldsymbol{I}\|_0$ decreases, the number of endmembers in $\boldsymbol{A_I}$ is still more than the number of true endmembers in $\boldsymbol{Y}$, and the unmixing error RSE1 will gradually increase, but the error growth rate will be very slow. When the number of endmembers

---

Algorithm 2 Local Search Operator

Input: Endmember selection vector $\boldsymbol{I}$

Output: Optimized vector $\boldsymbol{I}$

If $\boldsymbol{I}$ is entirely zero, it means no endmembers have been selected. Do not perform optimization and directly return.
if the zero-setting probability λ_2 is satisfied **then**
  Use $\boldsymbol{I}$ to select the endmember matrix $\boldsymbol{A_I}$ from the spectral library $\boldsymbol{A}$.
  Compute the matrix $\boldsymbol{X_I}$ corresponding to $\boldsymbol{A_I}$.
  Compute the $\boldsymbol{l_2}$-norm for each row of the abundance matrix $\boldsymbol{X_I}$.
  $\boldsymbol{j} = \arg\min_{\boldsymbol{i}} \|\mathbf{X_{I}}_{\boldsymbol{i}}\|_2$
  $\boldsymbol{I_j} \leftarrow 0$.
end if
Return the final optimized vector $\boldsymbol{I}$.

---

in $\boldsymbol{A_I}$, determined by $\|\boldsymbol{I}\|_0$, approaches the number of true endmembers in $\boldsymbol{Y}$, the unmixing error RSE1 will increase, and the error growth rate will increase significantly. When $\|\boldsymbol{I}\|_0$ is small, the number of endmembers in $\boldsymbol{A_I}$ cannot fully reflect the number of true endmembers in $\boldsymbol{Y}$, resulting in a very large unmixing error RSE1 and a very large error growth rate. Therefore, on the Pareto front of the two objectives of model (5), the unmixing error RSE1 will show a trend of rapidly decreasing first and then slowly decreasing as $\|\boldsymbol{I}\|_0$ increases. The number of endmembers can be determined by identifying the knee point on the Pareto front. Additionally, this paper designs a voting mechanism based on the Pareto solution set to identify the most significant endmembers. The core idea of this mechanism is to perform a statistical analysis of the endmember selection across all solutions within the Pareto solution set. Higher weights are assigned to solutions near the knee point on the left side (since the endmembers selected by these solutions lead to a rapid decrease in unmixing error RSE1, indicating their strong representational ability for the image). Subsequently, the frequency of each endmember being selected across all solutions is calculated, which is then used to measure its contribution to the solution set. Finally, based on the predetermined number of endmembers, the endmember set with the highest selection frequencies is chosen as the final solution. This voting mechanism is illustrated in Fig. III-C, and it integrates the selection information from multiple Pareto optimal solutions, avoiding the limitations of relying on a single solution and enhancing the robustness and representativeness of the identified endmembers.

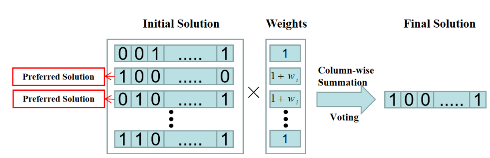

Fig. 2. Illustration on the voting solution strategy

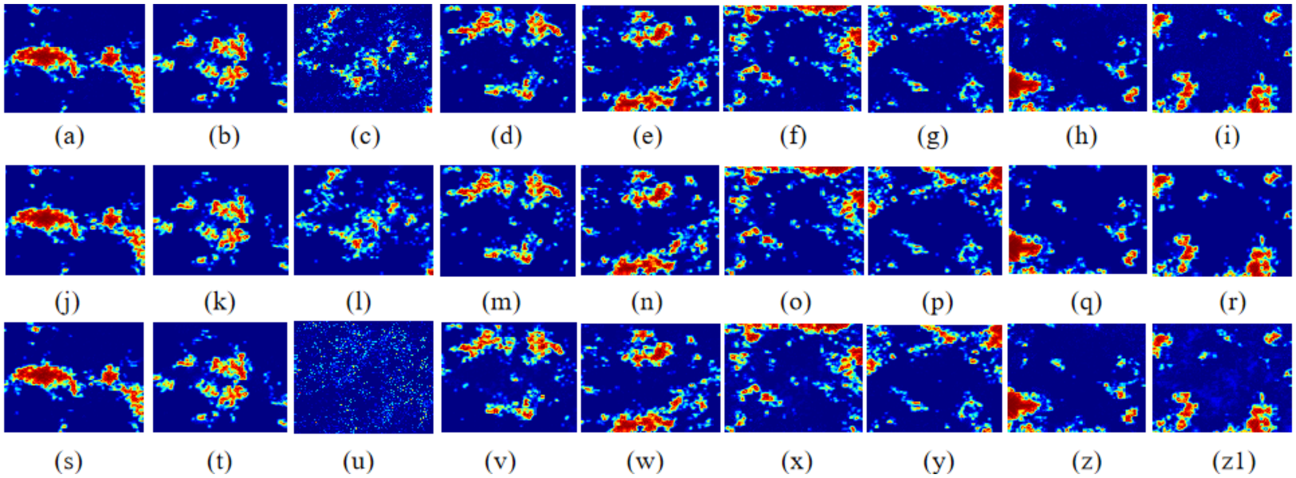

Fig. 3. The synthetic dataset. (a)-(i): Abundance Estimation Results Using MOEA/DL. (j)-(r): True abundance maps of nine endmembers. (s)-(z1): Abundance Estimation Results Using MOEA/D.

IV. EXPERIMENTS

A. Data Sets and Parameter Settings

This paper evaluates the performance of the unmixing algorithm using the synthetic dataset and the real hyperspectral dataset, i.e., Urban. The synthetic data is constructed as in [19]. The Urban dataset is one of the commonly used datasets in hyperspectral image unmixing research. The image has 307×307 pixels, with each pixel corresponding to a 2×2 square meter area. The dataset covers wavelengths ranging from 400 nm to 2500 nm, with a total number of 210 spectral bands and a spectral resolution of 10 nm. During preprocessing, channels significantly affected by atmospheric interference are typically removed, including bands 1 to 4, 76, 87, 101 to 111, 136 to 153, and 198 to 210. The remaining 162 bands are used for subsequent analysis. The over-complete spectral library used in this paper is the urban pixels.

Spectral similarity is a key quantitative metric for comparing two spectral vectors. In hyperspectral unmixing, common spectral similarity measures include root mean square error (RMSE) and spectral angle distance (SAD), defined as follows:

$$d_{\text{RMSE}} = \sqrt{1/N \sum\nolimits_{n=1}^{N} (\boldsymbol{a_i} - \boldsymbol{\hat{a}_i})^2} \tag{11}$$

$$d_{\text{SAD}} = \frac{1}{p} \sum_{i=1}^{i} \arccos\left(\frac{\hat{\mathbf{y}}_i^T \mathbf{y}_i}{\|\hat{\mathbf{y}}_i\| \cdot \|\mathbf{y}_i\|} \right) \tag{12}$$

where $\boldsymbol{\hat{a}_i}$ and $\boldsymbol{a_i}$ represent the estimated and true abundance vectors, respectively; $\boldsymbol{y_i}$ and $\boldsymbol{\hat{y}_i}$ are spectral vectors of the same structure. RMSE quantifies the difference between abundance vectors, while SAD measures the angular difference between spectral vectors. Lower values of both metrics indicate better performance.

This paper focuses on improving the endmember identification algorithm. To evaluate the accuracy of endmember estimation, two metrics are used: Correct Estimation Rate (CER) and Average Number of Correct Estimations (ANCE). CER measures the probability of fully estimating the number of endmembers in multiple experiments, representing the overall capability of endmember estimation. A larger CER value indicates that more endmembers are correctly identified during the experiments, which generally reflects higher accuracy and robustness of the model or algorithm for endmember estimation tasks. The ANCE metric describes the average number of successfully estimated endmembers in each experiment. This metric provides a relatively quantitative perspective to assess the model's accuracy in estimating endmembers within a single experiment. The closer the ANCE value is to the true value and the more stable it remains at the true value, the better the stability of the model. The formulas are as follows

$$\text{CER} = \text{NC}/\text{NT} \tag{13}$$

$$\sum\nolimits_{n=1}^{\text{NT}} N_n/\text{NT} \tag{14}$$

where NC refers to the number of times all endmembers were accurately estimated in multiple experiments, NT refers to the number of experiments, N_n denotes the number of endmembers accurately estimated in the n-th experiment.

Experiment results compare the MOEA/D-based unmixing method, the MOEA/D unmixing method with a local search operator, the NFINDR method [25], the vertex component analysis (VCA) method [24], the energy based convex set (ECS) method [26] and the PCOMMEND method [22].

The parameter settings for the MOEA/D in this experiment are as follows. The maximum number of iterations $gen = 230$, the neighborhood size $T = 10$, the population size $pop = 200$, the crossover probability is 1, and the mutation probability is $1/q$. Each algorithm was independently run $\text{NT} = 7$ times.

B. Analysis of Experimental Results

Fig. 3 presents the results on the synthetic dataset. The MOEA/D shows limitations in the accuracy of detail estimation under the influence of noise, with the effects being particularly evident in (u) and (z1). After incorporating the local search operator, the estimation of detailed information becomes more accurate.

TABLE I
COMPARISON OF MOEA/D ALGORITHM WITH AND WITHOUT THE LOCAL SEARCH OPERATOR

	p[1]	CER	ANCE	NT
MOEA/D	9	0.86	8.86	7
MOEA/DL[2]	9	**1**	**9**	7

[1] p represents the true number of endmembers.
[2] MOEA/DL represents the MOEA/D with Local Search Operator.

TABLE II
COMPARISON OF RMSE AND SAD ACROSS DIFFERENT ALGORITHMS

Algorithm	**RMSE** ($d_{\mathbf{RMSE}}$)	**SAD** ($d_{\mathbf{SAD}}$)
MOEA/D	0.309	0.244
MOEA/DL	**0.241**	**0.189**
NFINDR	0.310	0.236
VCA	0.297	0.212
ECS	0.290	0.272
PCOMMEND	0.322	0.310

Table I and II present the performance of various algorithms. Table I, shows that MOEA/DL accurately estimates the set of true endmembers in hyperspectral data, exhibiting high stability. In contrast, MOEA/D exhibits slight fluctuations and instability in estimating the true endmember set, highlighting the positive effect of the local search operator. Table II demonstrates that MOEA/DL achieves significant advantages over other common algorithms, with both SAD and RMSE values being lower than those of the compared methods.

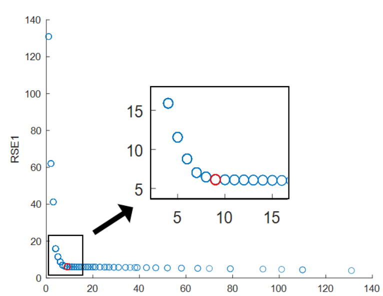

Fig. 4. Pareto solutions obtained by MOEA/DL, where SP1 is the number of selected endmembers and RSE1 is the reconstruction error.

Fig. 5 compares the endmember extraction results of MOEA/D and MOEA/DL. It can be observed that, for the same number of endmembers (identical SP1-axis values), MOEA/DL sometimes achieves a lower unmixing error (RSE1). Fig. 6 presents a comparison between the abundance maps obtained on the endmembers estimated by MOEA/D and MOEA/DL, and the ground truth abundance maps are also presented for comparison. From the figure, it can be observed that MOEA/D introduces some distortions compared to the ground truth abundance maps, with noticeable misjudgments in certain areas. By incorporating the local search operator, MOEA/DL achieves a significant improvement. The refinement brought by the local search operator effectively reduces unmixing differences and enhances the consistency between the estimated abundance maps and the ground truth maps. As a result, the abundance maps of the endmembers identified by MOEA/DL are visually closer to the ground truth maps, demonstrating the superior performance of MOEA/DL in handling challenging regions.

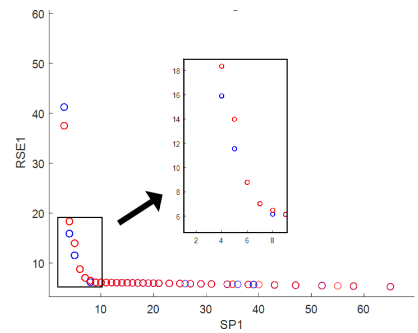

Fig. 5. Comparison of Pareto solutions obtained by MOEA/D and MOEA/DL. Blue circles denote MOEA/DL, and red circles denote MOEA/D.

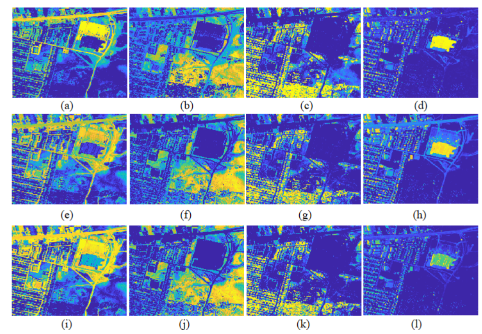

Fig. 6. The Urban dataset. (a)-(d): True abundance maps. (e)-(h): Abundance maps by MOEA/DL. (i)-(l): Abundance maps by MOEA/D.

V. CONCLUSION

This paper proposes a memetic hyperspectral unmixing method under the MOEA/D framework, which combines global search and local search to enhance the performance of endmember extraction and abundance estimation. First, a local search operator is designed under the MOEA/D framework, enabling individuals to fully utilize their abundance information during the evolution process, thereby improving the accuracy of endmember extraction. Second, a voting mechanism based on the Pareto solution set is introduced, which integrates the identification knowledge from multiple optimal solutions. The endmember set with the highest frequency is selected as the final solution, mitigating the instability that might arise from relying solely on a single Pareto optimal solution. Finally, experiments on both synthetic and real datasets demonstrate the superiority of the proposed method in endmember extraction and abundance estimation. The proposed method provides a new perspective on the integration of evolutionary multi-objective optimization algorithms with hyperspectral data processing knowledge. Future work will further explore the information available during evolution process to enhance the efficiency of the algorithm.

REFERENCES

[1] Tong Q X, Zhang B, Zhang L F. Current progress of hyperspectral remote sensing in China[J]. Journal of Remote Sensing, 2016, 20(5): 689-707.

[2] Keshava N, Mustard J F. Spectral unmixing[J]. IEEE Signal Processing Magazine, 2002, 19(1): 44-57.

[3] Bioucas-Dias J M, Plaza A, Dobigeon N, et al. Hyperspectral unmixing overview: Geometrical, statistical, and sparse regression-based approaches[J]. IEEE Journal of Selected Topics in Applied Earth Observations and Remote Sensing, 2012, 5(2): 354-379.

[4] WANG W, QIAN Y, LIU H. Multiple clustering guided nonnegative matrix factorization for hyperspectral unmixing [J]. IEEE Journal of Selected Topics in Applied Earth Observations and Remote Sensing, 2020, 13: 5162-5179.

[5] Heylen R, Parente M, Gader P. A review of nonlinear hyperspectral unmixing methods[J]. IEEE Journal of Selected Topics in Applied Earth Observations and Remote Sensing, 2014, 7(6): 1844-1868.

[6] Feng X R, Li H C, Wang R, et al. Hyperspectral unmixing based on nonnegative matrix factorization: A comprehensive review[J]. IEEE Journal of Selected Topics in Applied Earth Observations and Remote Sensing, 2022, 15: 4414-4436.

[7] ZHOU L, ZHANG X, WANG J, et al. Subspace structure regularized nonnegative matrix factorization for hyperspectral unmixing [J]. IEEE Journal of Selected Topics in Applied Earth Observations and Remote Sensing, 2020, 13: 4257-4270.

[8] Zhang S, Zhang G, Li F, et al. Spectral-spatial hyperspectral unmixing using nonnegative matrix factorization[J]. IEEE Transactions on Geoscience and Remote Sensing, 2021, 60: 1-13.

[9] Rasti B, Hong D, Hang R, et al. Feature extraction for hyperspectral imagery: The evolution from shallow to deep: Overview and toolbox[J]. IEEE Geoscience and Remote Sensing Magazine, 2020, 8(4): 60-88.

[10] Su Y C, Xu R Q, Gao L R, et al. Development of deep learning-based hyperspectral remote sensing image unmixing[J]. National Remote Sensing Bulletin[in Chinese], 2024, 28(1): 1-19.

[11] Chen J, Zhao M, Wang X, et al. Integration of physics-based and data-driven models for hyperspectral image unmixing: A summary of current methods[J]. IEEE Signal Processing Magazine, 2023, 40(2): 61-74.

[12] Zheng P, Wu Z, Paoletti M E, et al. Typical mineral abundance estimation of Chang'e-3 Yutu Rover with hyperspectral data based on diffusion autoencoder unmixing model[C]//IGARSS. IEEE, 2024: 6109-6112.

[13] Gao L, Han Z, Hong D, et al. CyCU-Net: Cycle-consistency unmixing network by learning cascaded autoencoders[J]. IEEE Transactions on Geoscience and Remote Sensing, 2021, 60: 1-14.

[14] Su Y, Li J, Plaza A, et al. DAEN: Deep autoencoder networks for hyperspectral unmixing[J]. IEEE Transactions on Geoscience and Remote Sensing, 2019, 57(7): 4309-4321.

[15] Li H, Li D, Gong M, et al. Sparse hyperspectral unmixing with preference-based evolutionary multiobjective multitasking optimization[J]. IEEE Transactions on Emerging Topics in Computational Intelligence, 2024, 8(2): 1922-1937.

[16] Song M, Zhong Y, Ma A, et al. Multiobjective spatiotemporal subpixel mapping for remote sensing imagery[J]. IEEE Transactions on Geoscience and Remote Sensing, 2024, 62: 1-17.

[17] Neri F, Cotta C. Memetic algorithms and memetic computing optimization: A literature review[J]. Swarm and Evolutionary Computation, 2012, 2: 1-14.

[18] Ghosh A, Kalidindi R S A. Enhancing CNN classification with Lamarckian memetic algorithms and local search[C]//2024 International Conference on Signal Processing and Advance Research in Computing (SPARC). IEEE, 2024, 1: 1-7.

[19] Jiang X , Gong M , Li H ,et al. A two-phase multiobjective sparse unmixing approach for hyperspectral data[J]. IEEE Transactions on Geoscience and Remote Sensing. 2018, 56(1): 508-523.

[20] Yao F, Chen H, Liu X, et al. A multi-objective memetic algorithm for workflow scheduling in clouds[J]. IEEE Transactions on Emerging Topics in Computational Intelligence, 2024. doi: 10.1109/TETCI.2024.3462856.

[21] Ma A, Zhou W, Song M, et al. Multiobjective memetic spatiotemporal subpixel mapping for remote sensing imagery[J]. IEEE Transactions on Geoscience and Remote Sensing, 2023, 61: 1-18.

[22] Zare A, Gader P, Bchir O, et al. Piecewise convex multiple-model endmember detection and spectral unmixing[J]. IEEE Transactions on Geoscience and Remote Sensing, 2012, 51(5): 2853-2862.

[23] Iordache M D, Bioucas-Dias J M , Plaza A .Total variation spatial regularization for sparse hyperspectral unmixing[J]. IEEE Transactions on Geoscience and Remote Sensing, 2012, 50(11): 4484-4502.

[24] Nascimento J M P, Dias J M B .Vertex component analysis: A fast algorithm to unmix hyperspectral data[J]. IEEE Transactions on Geoscience and Remote Sensing, 2005,43(2):898-910.

[25] Winter M E. N-FINDR: An algorithm for fast autonomous spectral end-member determination in hyperspectral data[C]. Proceedings of SPIE, 1999, 3753: 266-275.

[26] Shah, D., Zaveri, T. Energy based convex set hyperspectral endmember extraction algorithm[C]. Computer Vision and Image Processing, 2019,1147: 51-60.